Journal of Medicinal Chemistry

Article

Cite This: J. Med. Chem. 2018, 61, 4103−4114

pubs.acs.org/jmc

An ^{18}F-Labeled Poly(ADP-ribose) Polymerase Positron Emission Tomography Imaging Agent

Filip Zmuda,[*,†,‡] Adele Blair,[†] Maria Clara Liuzzi,[†,§] Gaurav Malviya,[⊥] Anthony J. Chalmers,[‡] David Lewis,[⊥] Andrew Sutherland,[†] and Sally L. Pimlott[#]

[†]WestCHEM, School of Chemistry, University of Glasgow, The Joseph Black Building, Glasgow G12 8QQ, U.K.

[‡]Wolfson Whol Cancer Research Centre, Institute of Cancer Sciences, University of Glasgow, Glasgow G61 1QH, U.K.

[§]School of Medicine, College of Medical, Veterinary and Life Sciences, University of Glasgow, Glasgow G12 8QQ, U.K.

[⊥]Cancer Research UK Beatson Institute, Glasgow G61 1BD, U.K.

[#]West of Scotland PET Centre, Greater Glasgow and Clyde NHS Trust, Glasgow G12 0YN, U.K.

Supporting Information

ABSTRACT: Poly(ADP-ribose) polymerase (PARP) is involved in repair of DNA breaks and is over-expressed in a wide variety of tumors, making PARP an attractive biomarker for positron emission tomography (PET) and single photon emission computed tomography imaging. Consequently, over the past decade, there has been a drive to develop nuclear imaging agents targeting PARP. Here, we report the discovery of a PET tracer that is based on the potent PARP inhibitor olaparib (**1**). Our lead PET tracer candidate, [^{18}F]**20**, was synthesized and evaluated as a potential PARP PET radiotracer in mice bearing subcutaneous glioblastoma xenografts using ex vivo biodistribution and PET−magnetic resonance imaging techniques. Results showed that [^{18}F]**20** could be produced in a good radioactivity yield and exhibited specific PARP binding allowing visualization of tumors over-expressing PARP. [^{18}F]**20** is therefore a potential candidate radiotracer for in vivo PARP PET imaging.

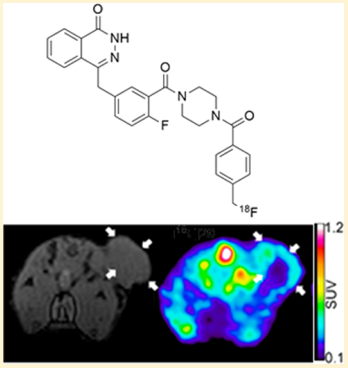

INTRODUCTION

Poly(ADP-ribose) polymerase-1 (PARP-1) is a nuclear protein that exhibits a broad range of functions and is involved in transcription, mitosis, apoptosis, and DNA damage repair.[1,2] PARP inhibition has been investigated as a therapeutic approach to treat cancers by either synthetic lethality in which tumor cells deficient in a type of DNA repair termed homologous recombination are sensitized to PARP inhibition, or chemoradiosensitization, in which PARP inhibition sensitizes tumor cells to conventional chemo- or radiotherapy. To date, olaparib (Lynparza), niraparib (Zejula), and rucaparib (Rubraca) are the only PARP inhibitors to receive approval for clinical use in the United States or Europe.[3,4] Olaparib (**1**; Figure 1) was the first agent in its class to receive such approval. In the European Union, it is currently indicated for the treatment of BRCA-mutated (homologous recombination deficient) ovarian, fallopian-tube, and peritoneal cancers,[4] in which it has been shown to increase progression-free[5] and overall[6] survival. In the United States, **1** can also be used for treatment of BRCA-mutated metastatic breast cancer[7] and as a maintenance therapy for patients with platinum-sensitive recurrent epithelial ovarian, fallopian-tube, or primary peritoneal cancer irrespective of BRCA mutations.[8] In both cases, **1** was once again shown to increase progression-free survival.[9,10]

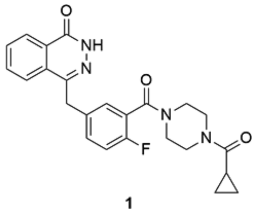

1

Figure 1. PARP inhibitor olaparib.

Olaparib **1** is also being investigated as a radio- and chemosensitizer for the treatment of solid cancers, including gliomas. However, adding PARP inhibitors to cytotoxic chemotherapy agents has been shown to exacerbate bone marrow toxicity in humans, hindering the establishment of effective PARP inhibitor and chemotherapy dosage regimens with acceptable safety profiles.[11] In the case of brain tumors, matters are further complicated as **1** suffers from poor blood−brain barrier (BBB) permeability, and delivery of the drug to the tumor is reliant on BBB disruption.[12] The degree of BBB disruption in brain tumors is very variable;[13−15] this could affect tumor penetration by **1** and, hence, reduce the clinical effectiveness of PARP inhibitor therapy. Furthermore, in vivo animal studies have revealed that prolonged treatment with **1**

Received: January 26, 2018
Published: April 9, 2018

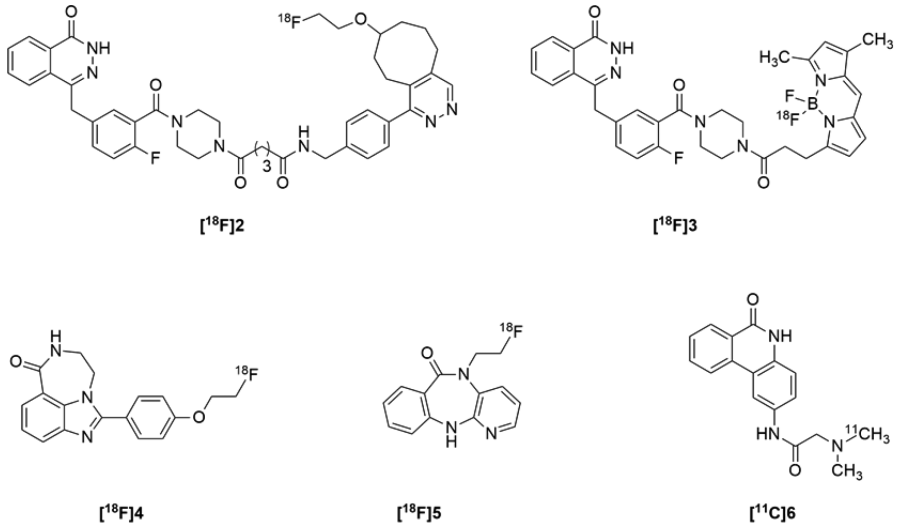

Figure 2. Published examples of PARP PET radiotracers.[22,23]

can result in increased tumor *P*-glycoprotein efflux transporter expression and subsequent drug resistance.[16]

The above-mentioned issues highlight the challenges that are associated with PARP inhibitor therapy in the context of synthetic lethality as well as chemo- and radiosensitization. Nuclear imaging of an appropriately radiolabeled PARP inhibitor could be used to overcome these challenges. In combination with a suitable blockade study protocol, nuclear imaging could indirectly establish the distribution and retention of PARP inhibitors in tumors and normal tissues and subsequently identify therapeutic dosage regimens for which the combination of PARP inhibitors and cytotoxic agents exerts maximal tumor and minimal bone marrow cytotoxicity. Furthermore, a radiolabeled PARP probe could be used to indirectly ascertain the occupancy, retention, and target engagement of **1** in brain tumor tissue. This type of approach has been successfully applied in preclinical models of small-cell lung[17] and epithelial ovarian cancer.[18] In a clinical setting, this could be used to identify patients that are unlikely to respond to PARP inhibitor therapy due to weak target engagement as a consequence of poor drug tumor uptake or resistance caused by efflux transporter over-expression.

Previously, we reported the synthesis and characterization of a [^{123}I]-labeled compound with potential for single-photon emission computed tomography (SPECT) imaging of PARP.[19] Despite the established nature of the SPECT imaging modality, the use of positron emission tomography (PET) is rapidly expanding and, in many cases, has become the preferred nuclear imaging modality in the clinic. This can be attributed to the superior spatial resolution,[20] quantification, and sensitivity[21] of PET compared to SPECT. It is, therefore, not surprising that many of the current nuclear imaging agents for PARP were designed with PET imaging in mind (Figure 2).[22,23] Importantly, the rationale for developing PARP PET imaging agents has been recently solidified by [^{18}F]**4**, which was shown to be capable of noninvasively ascertaining PARP-1 expression in epithelial ovarian tumors in humans.[18,24]

Here, we report the synthesis of a small library of fluorinated analogs of the clinical PARP inhibitor **1** with potential for PARP PET imaging and the in vitro characterization of these compounds. The lead analog **20** was synthesized in its radiofluorinated version and evaluated as a potential PARP PET radiotracer in mice bearing subcutaneous glioblastoma xenografts using ex vivo biodistribution and PET−magnetic resonance (MR) imaging techniques.

RESULTS AND DISCUSSION

Chemistry and in Vitro Characterization. Due to poor accessibility of the central ring fluorine atom of **1** for radiolabeling,[25] focus was directed at synthesizing analogs of **1** bearing distal fluorinated moieties that were more likely to be amenable to radiofluorination methods. Initially, six fluorinated PARP inhibitors (**8**−**13**) containing the characteristic phthalazinone scaffold were synthesized through amide or *N*-alkyl coupling of commercially available benzoic carboxylic acids or benzyl halides with piperazine **7**, the synthesis of which we described previously[19] (Table 1). The structures of compounds **8**−**13** were confirmed in part by nuclear magnetic resonance (NMR) spectroscopic analysis, which showed that the majority of these exist as a mixture of amide rotamers. The design of these analogs was partly driven by previous reports,[25−27] which have shown that structural modifications can be performed in the cyclopropane bearing region of **1** without having a marked effect on PARP inhibition. To confirm this, cell-free PARP-1 IC_{50} assays were performed on compounds **8**−**13**, and the results of these experiments were compared against the cell-free IC_{50} of **1** (Table 1). Compared to **1**, all compounds showed improved PARP-1 potency except for compound **13**, which had an overlapping cell-free IC_{50} 95% confidence interval. Compounds **8**−**13** were also evaluated for their lipophilic and plasma protein binding properties, defined by log P_{oct} and percentage plasma protein binding (%PPB) parameters (Table 1). All six analogs exhibited greater log P_{oct} and %PPB values in comparison to **1**. This may be attributed to the addition of aromatic and methyl moieties, which have the potential to increase lipophilicity and can, in turn, result in an increased % PPB due to the hydrophobic nature of plasma protein interactions.[28] From the perspective of nuclear imaging, radiotracers with high log P_{oct} (>3.0)[29] and %PPB (>95%)[30] values can be associated with poor passive diffusion across biological membranes and vascular retention, which can in turn result in a poor target to background signal ratio. The physiochemical parameters of **8**−**12** were all found to be within the optimal range for radiotracer development.

DOI: 10.1021/acs.jmedchem.8b00138
J. Med. Chem. 2018, 61, 4103−4114

Table 1. Methods Used to Generate Analogs 8−13 from the Penultimate Compound 7 as well as the Cell-Free PARP-1 Inhibitory and Physiochemical Properties of 1 and 8−13

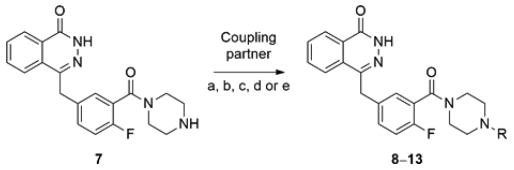

7 8–13

Coupling partner	Coupling conditions	R	Yield, %	Cell-free IC_{50} (95% CI), nM[a]	Log P_{oct}[b]	%PPB[c]
	a	 1	51	11.9 (10.5–13.6)	1.95	75.9
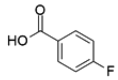	b	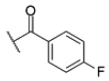 8	75	5.9 (4.9–7.0)	2.51	85.9
	b	 9	53	3.6 (3.4–3.9)	2.46	86.4
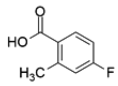	c	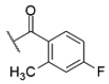 10	31	2.9 (2.3–3.7)	2.66	86.1
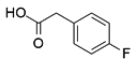	d	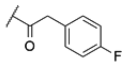 11	46	1.3 (0.9–1.7)	2.67	89.9
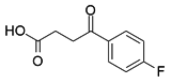	c	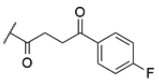 12	34	4.1 (3.6–4.6)	2.81	90.6
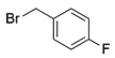	e	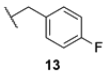 13	38	11.2 (7.3–17.3)	3.14	94.7

[a]Cell-free IC_{50} values are based on three experiments. [b]Lipophilicity (log P_{oct}) was determined using a C-18 reverse-phase HPLC column. [c]Percentage plasma protein binding (%PPB) was determined using a human serum albumin coated HPLC column. Reagents and conditions for reaction below the table title: (a) HBTU, Et_3N, DMF, room temperature (rt), 72 h; (b) HBTU, DIPEA, CH_2Cl_2, rt, 24 h; (c) EDCl, DMAP, CH_2Cl_2, rt then reflux, 24 h; (d) HBTU, DIPEA, DMF, 50 °C, 24 h; (e) DIPEA, CH_2Cl_2, rt, 24 h.

However, following analysis of the established in vitro parameters and potential radiochemical accessibility, compound **8** was identified as an initial lead candidate for further advancement in this research program. To establish the potency of **8** against PARP in living cells, cellular IC_{50} assays were performed using primary (G7) and secondary (T98G) human glioblastoma cell lines (Table 2) and previously described methodology.[19] Compound **8** exhibited low nanomolar IC_{50} values that were in line with those observed for **1** in both cell lines, suggesting that **8** was able to effectively penetrate cellular membranes and reach PARP localized within cellular nuclei.

Table 2. Cellular PARP Inhibitory Properties of Compounds 1 and 8

compound	cellular IC_{50} (95% CI), nM[a]	
	G7	T98G
1	1.6 (1.4−1.8)	1.6 (1.4−1.8)
8	1.0 (0.9−1.2)	0.8 (0.7−0.9)

[a]Cellular IC_{50} values obtained using primary G7 and established T98G human glioblastoma cell lines are based on two experiments.

To access the [^{18}F]-radiofluorine analog of **8**, standard aromatic nucleophilic substitution chemistry was employed using *p*-nitrobenzamide precursor **14**, which was generated through amide coupling of **7** with commercially available 4-nitrobenzoic acid (Scheme 1). However, optimization of the radiofluorination step proved challenging (see the Supporting Information), and the maximum radiochemical yield (based on high-performance liquid chromatography [HPLC] analysis of crude product) achieved was only 19% (Scheme 1). It was proposed that the poor yield was a consequence of a lack of activation of the system for aromatic nucleophilic substitution due to the weak electron withdrawing properties of the amide located *para*- to the nitro leaving group. Since commencing this work, Carney et al. were able to synthesize [^{18}F]**8** with an optimized radioactivity yield of 38 ± 2.5% (isolated product)

DOI: 10.1021/acs.jmedchem.8b00138
J. Med. Chem. 2018, 61, 4103−4114

Scheme 1. Radiofluorination Approach Used to Generate [^{18}F]8 From the Nitro Precursor 14

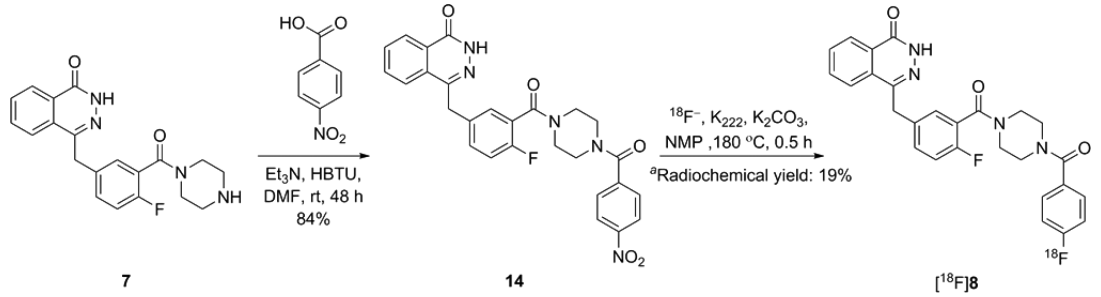

[a]Radiochemical yield was determined by radio-HPLC analysis of the crude product.

Scheme 2. Synthetic Route Used to Generate Compound 20

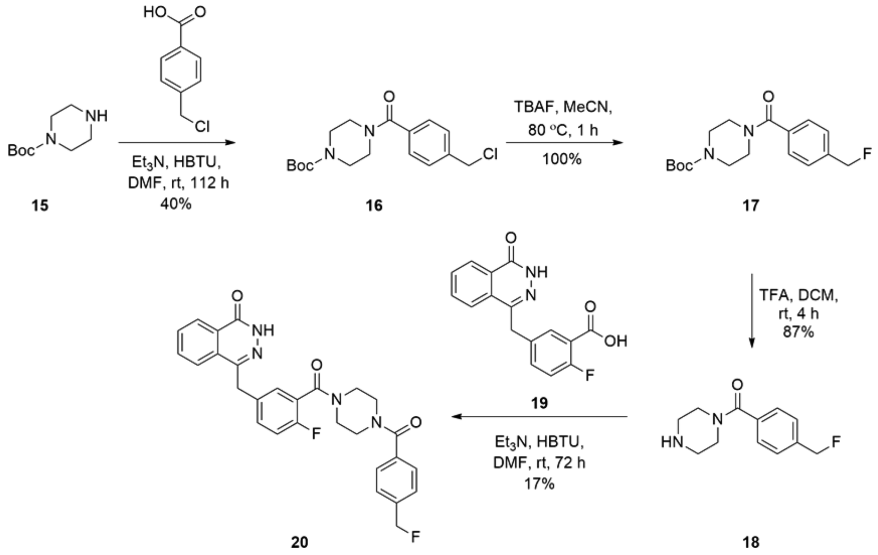

Table 3. Physiochemical, Cell-Free PARP-1 and Cellular PARP Inhibitory, and Mouse Plasma and Metabolic Stability Properties of 1 and 20

				cellular IC_{50} (95% CI), nM[d]		plasma stability, percent[e]		Cl_{int}, μL min^{-1}mg^{-1}[f]	
compound	log P_{oct}[a]	%PPB[b]	cell-free IC_{50} (95% CI), nM[c]	G7	T98G	0 h	20 h	experiment 1	experiment 2
1	1.95	75.9	11.9 (10.5−13.6)	1.6 (1.4−1.8)	1.6 (1.4−1.8)	–	–	23	34
20	2.51	89.3	2.0 (1.9−2.2)	1.3 (0.7−2.3)	2.0 (1.3−3.1)	93	95	74	90

[a]Lipophilicity (log P_{oct}) was determined using a C-18 reverse-phase HPLC column. [b]Percentage plasma protein binding (%PPB) was determined using a human serum albumin coated HPLC column. [c]Cell-free IC_{50} values are based on three experiments. [d]Cellular IC_{50} values obtained using primary G7 and established T98G human glioblastoma cell lines are based on two experiments. [e]The mean percentage of parent compound remaining after a 20 h incubation in mouse plasma (±SD of 3 experiments) was ascertained for compound **20**. [f]Intrinsic clearance (Cl_{int}) values of two independent experiments acquired using human liver microsomes.

using a multistep early-stage radiofluorination approach that circumvented the aforementioned issue of poor activation.[17] Therefore, our attention was redirected toward an alternative target compound, **20**, bearing a *p*-(fluoromethyl)benzamide group. It was proposed that a precursor analog of **20** would be more amenable to radiofluorination than *p*-nitrobenzamide **14**, thereby allowing for late-stage radiofluorination and radiosynthetic automation. Compound **20** was synthesized by first performing an amide coupling reaction between mono-Boc protected piperazine **15** and commercially available 4-(chloromethyl)benzoic acid, giving access to intermediate **16** in 40% yield (Scheme 2). *p*-Chlorobenzamide **16** was then subjected to nucleophilic fluorination with tetra-*n*-butylammonium fluoride (TBAF), and this was followed by acid-mediated cleavage of the Boc-protecting group to give **18** in 87% yield over two steps. Finally, reaction of carboxylic acid **19**, previously synthesized within our research group,[19] and piperazine **18** under standard amide coupling conditions gave target **20**. The log P_{oct}, %PPB, and cell-free and cellular IC_{50} values were established for **20** in the same manner as described for the other analogs (**8**−**13**) in this series (Table 3).

As expected, compound **20** exhibited higher log P_{oct} and %PPB values than **1** (Table 3). However, these were still within the optimal range for a nuclear imaging agent. Interestingly, despite **20** having an identical log P_{oct} value to **8**, the former compound exhibited a higher degree of %PPB. Furthermore,

DOI: 10.1021/acs.jmedchem.8b00138
J. Med. Chem. 2018, 61, 4103−4114

compound **20** had a cell-free IC_{50} value that was 6- and 3-fold less than that acquired for **1** and **8**, respectively. Conversely, the cellular PARP inhibitory properties of **20** were comparable to compound **1** and marginally weaker than ascertained for compound **8**. Collectively, the optimal physiochemical properties and low nanomolar PARP cell-free and cellular IC_{50} values supported further investigation of **20** as a potential radiotracer for PARP. In the body, radiotracers can be exposed to a number of metabolic pathways, including blood plasma hydrolysis and liver functionalization or conjugation reactions that can have a significant effect on the kinetic properties of the tracer and, subsequently its usefulness in nuclear imaging. With this in mind, the in vitro plasma and liver microsome stability of lead candidate **20** were established by incubating the compound in mouse plasma proteins and human liver microsome enzymes, respectively, using previously described methodologies.[19] Candidate **20** appeared stable in mouse plasma with negligible decomposition following a 20 h incubation (Table 3). However, the intrinsic clearance parameter (a predictor of phase I liver metabolism) was approximately 3-fold greater for compound **20** in comparison to **1**. Despite this, it was proposed that compound **20** would exhibit sufficient tissue retention to allow for nuclear imaging of PARP. This was justified by previously acquired data using a radioiodinated *p*-iodobenzamide analog that exhibited similar in vitro intrinsic clearance properties to **20** but still displayed a degree of retention in PARP over-expressing tumor tissue.[19]

Initial attempts to generate the radiofluorinated version of **20** involved performing nucleophilic substitution reactions between the $^{18}F^-$ nucleophile and the chloromethyl group of precursor **21**, which was obtained by amide coupling of **7** with commercially available 4-(chloromethyl)benzoic acid (Scheme 3). However, these attempts were not successful because competing oligomerization reactions between the chloromethyl group of **21** and the phthalazinone core prevented effective radiofluorination. To overcome this issue, the phthalazinone core of **21** was Boc-protected to give compound **22**.

Precursor **22** was then subjected to a screen of radiofluorination conditions as outlined in Table 4. The radiochemical yield (based on HPLC analysis of the crude product) was 30% when tetra-*n*-butylammonium hydrogen carbonate ($TBAHCO_3$) was used as a phase-transfer agent, which was markedly higher in comparison to that obtained for Kryptofix (K_{222}) (entries 1 and 2). It has been reported in the literature that the introduction of a sterically hindered protic alcohol can have a beneficial effect on aliphatic nucleophilic radiofluorination reactions.[31,32] With the use of a 2:1 mixture of *t*-BuOH and MeCN as the reaction solvent, the radiofluoride incorporation increased from 30% to 48% in comparison to the same volume of MeCN alone (entries 1 and 3). A 30 min reaction time was established to be optimal based on lower radiochemical yields observed after a shorter reaction time (entry 4) and the short-lived nature of the ^{18}F radioisotope (half-life of 109.8 min), which prevented longer reaction periods. Radiofluoride incorporation was further improved by increasing the reaction temperature from 100 to 110 °C, which resulted in a 51% radiochemical yield (entry 5). Interestingly, doubling the reaction solvent volume had a negative impact on the degree of radiofluorination (entry 6). Based on these data, the reaction conditions described in entry 5 were deemed optimal.

To access [^{18}F]**20**, compound [^{18}F]**23** was subjected to Boc deprotection, which was achieved in 5 min and with minimal defluorination taking place by using water as an acid−base catalyst (Scheme 4). The use of hydrochloric acid was also investigated as a deprotecting agent, but its use was associated with marked defluorination (see the Supporting Information). The optimized two-step one-pot radiochemical reaction allowed access to [^{18}F]**20** in a radioactivity yield (isolated product) of 9 ± 2% (n = 7) and a molar activity of >4.32 ± 1.46 Ci μmol^{-1} (n = 3). Importantly, the one-pot nature of the reaction opens up the potential for radiosynthetic automation.

Scheme 3. Synthetic Route Used to Generate *p*-Chloromethylbenzamide Precursor 22

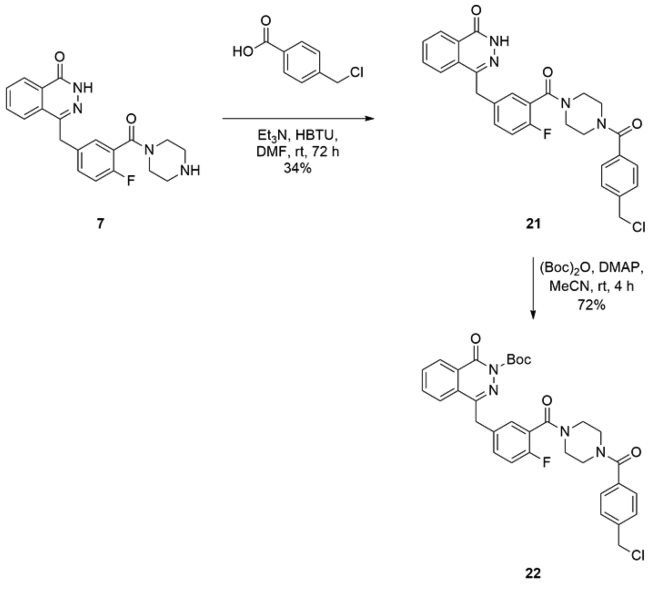

In Vivo Characterization. Following successful optimization of the radiochemistry, the behavior of [^{18}F]**20** was investigated in vivo in mice bearing subcutaneous U87MG-Luc2 human glioblastoma tumor xenografts using ex vivo biodistribution and PET−MR imaging techniques. Ex vivo biodistribution of [^{18}F]**20** was established at 30, 60, and 120 min after intravenous radiotracer administration, and PET data were acquired by performing a 45 min dynamic scan. These experiments showed that a large proportion of radioactivity was detectable in the liver and small bowel at 30−45 min post tracer administration (Figure 3a,b) and mostly concentrated in the cecum matter and solid feces after 120 min (Figure 3a). This is in line with our previous findings[19] and other literature reports,[25,33,34] which showed in vivo hepatobiliary clearance of a range of related radioiodinated and radiofluorinated compounds based on the structure of **1**. Interestingly, the mean percentage of injected dose per gram (%ID/g) of femur tissue remained relatively high across all three biodistribution time points (i.e., >8.5%; Figure 3a), which was also confirmed by PET imaging, in which high skeletal uptake of radioactivity was visible (Figure 3b). This is in contrast to observations made by Carney et al., who reported <2%ID/g of bone of [^{18}F]**8** at 120 min.[34] The high bone uptake seen with [^{18}F]**20** could be explained by in vivo defluorination and subsequent radiofluoride accumulation in bone tissue.[35] Despite this, apparent radiotracer tumor uptake was identified in both biodistribution and PET−MR imaging experiments (Figures 3a,c), whereas in the case of the former, the mean ratio of %ID/g of glioblastoma tumor to muscle increased from 1.9 ± 0.5 (n = 4) to 3.6 ± 0.5 (n = 4) between the 30 and 120 min time points. This was

DOI: 10.1021/acs.jmedchem.8b00138
J. Med. Chem. 2018, 61, 4103−4114

Table 4. Optimization of the Nucleophilic Halogen Exchange Methodology Used to Access Intermediate [^{18}F]23 from the Chloro Precursor 22

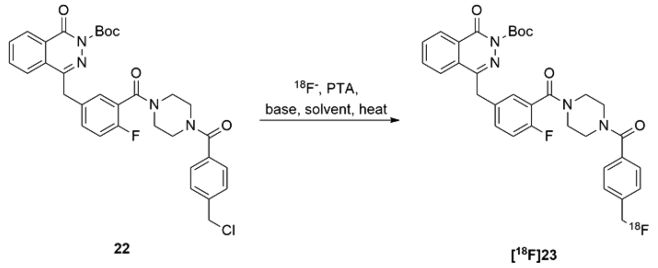

22 [^{18}F]23

entry	solvent (volume, mL)	PTA[a]	temperature, °C	reaction time, min	radiochemical yield, percent[b]
1	MeCN (0.3)	$TBAHCO_3$	100	30	30
2	MeCN (0.3)	K_{222}	100	30	4
3	MeCN (0.1)/ *t*BuOH (0.2)	$TBAHCO_3$	100	30	48
4	MeCN (0.1)/ *t*BuOH (0.2)	$TBAHCO_3$	100	10	22
5	MeCN (0.1)/ *t*BuOH (0.2)	$TBAHCO_3$	110	30	51
6	MeCN (0.2)/ *t*BuOH (0.4)	$TBAHCO_3$	110	30	37

[a]PTA: phase-transfer agent. [b]Radiochemical yields were determined by radio-HPLC analysis of the crude product from a single reaction.

Scheme 4. Optimized Radiofluorination Approach Used to Generate [^{18}F]20

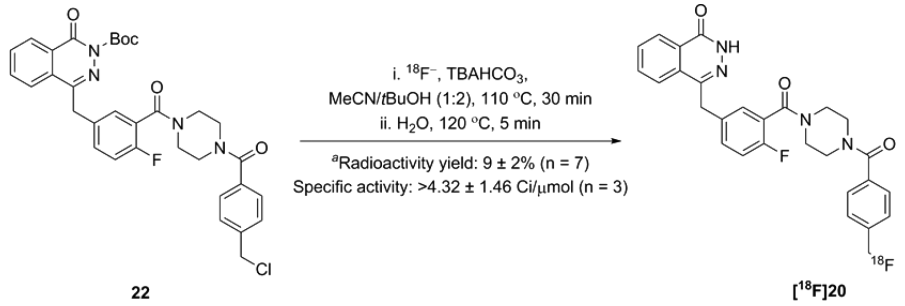

22 [^{18}F]20

[a]Radioactivity yield was determined using the measured radioactivity of the isolated product.

suggestive of [^{18}F]**20** retention in U87Mg-Luc2 glioblastoma tissue, which we have shown to be highly proliferative (see the Supporting Information) and to over-express PARP relative to muscle tissue (Figure 3d).

To establish the specificity of [^{18}F]**20** for PARP in bone and tumor tissue, further biodistribution studies were performed on subcutaneous U87MG-Luc2 glioblastoma bearing mice that had PARP binding sites blocked by pretreatment with nonradioactive compound **1** at a dose of 50 mg/kg 20 min prior to [^{18}F]**20** administration. The uptake of [^{18}F]**20** in bone tissue remained high 60 min after radioligand administration and was not influenced by the presence of excess nonradioactive **1** (Figure 3e). This supports the earlier proposed possibility of in vivo [^{18}F]**20** defluorination, leading to free radiofluoride accumulation in the bone. Despite this, preblockade using **1** resulted in a statistically significant decrease in the ratio of %ID/g of tumor to muscle from 1.79 ± 0.39 (n = 4) to 1.07 ± 0.15 (n = 4) 60 min after [^{18}F]**20** administration in comparison to vehicle-pretreated mice (unpaired t-test: $P < 0.05$). These findings suggested that the uptake of [^{18}F]**20** in tumor was due to specific PARP binding, which was in line with our previous findings for a related radioiodinated analog of **1**.[19]

CONCLUSIONS

We described here the identification and one-pot manual radiosynthesis of a PARP PET imaging agent, [^{18}F]**20**, that was accessed in good radioactivity yield and showed desirable physiochemical properties but suffered from rapid hepatobiliary clearance and in vivo defluorination followed by nonspecific $^{18}F^-$ bone tissue uptake in mice. Despite this, the radiotracer compound exhibited specific PARP binding and subcutaneous glioblastoma tumor retention properties, which allowed for preclinical PET visualization of the PARP over-expressing tumor. Therefore, we believe that [^{18}F]**20** should remain a potential candidate radiotracer for in vivo PARP PET imaging and that future imaging studies using small-animal intracranial glioblastoma models are required to further assess the utility of this compound.

EXPERIMENTAL SECTION

All reagents and starting materials were obtained from commercial sources and used as received. Dry solvents were purified using a solvent purification system, and all reactions were performed under an atmosphere of argon unless stated otherwise. Macherey-Nagel aluminum-backed plates precoated with silica gel 60F_{254} were used for thin layer chromatography and were visualized with a UV lamp. Flash column chromatography was performed using Fisher matrix silica gel 60 (35−70 μm). ^{1}H NMR spectra were recorded on a Bruker DPX 400 or Bruker 500 spectrometer, and data are reported as follows: chemical shift in parts per million (ppm) relative to Me_4Si or the solvent ($CDCl_3$, δ 7.26 ppm; CD_3OD, δ 3.31 ppm; or dimethyl sulfoxide [DMSO-δ_6] δ, 2.50 ppm) as the internal standard, multiplicity (s, singlet; d, doublet; t, triplet; q, quartet; m, multiplet or overlap of nonequivalent resonances, integration). ^{13}C NMR

DOI: 10.1021/acs.jmedchem.8b00138
J. Med. Chem. 2018, 61, 4103−4114

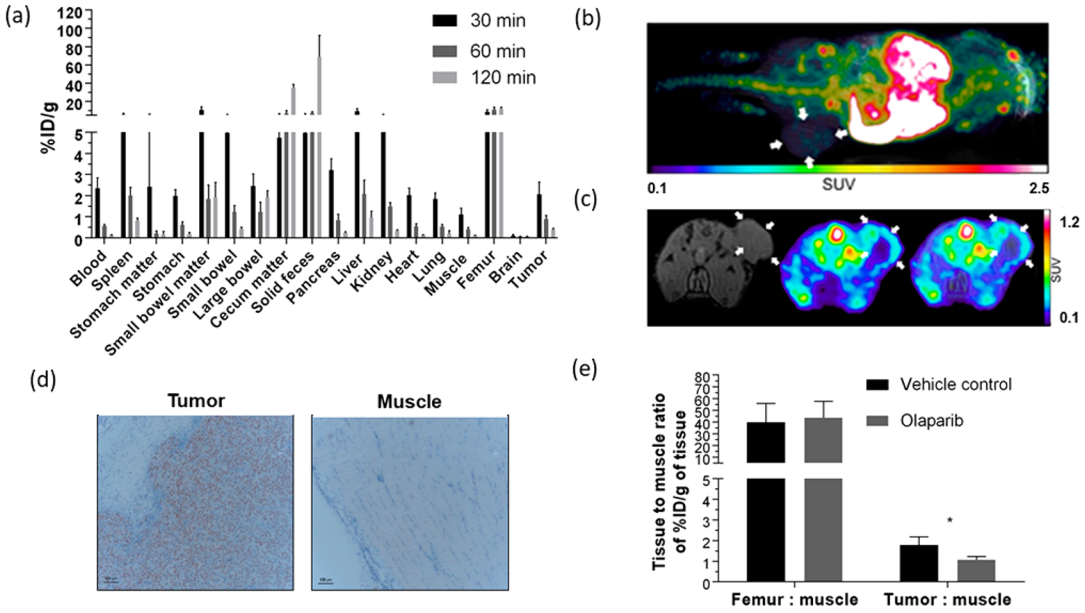

Figure 3. (a) Ex vivo biodistribution of [^{18}F]**20** in subcutaneous human U87MG-Luc2 glioblastoma bearing nude mice 30 min (n = 4), 60 min (n = 4), and 120 min (n = 4) after tracer injection (error bars represent the mean percentage of injected dose per gram of tissue or material (% ID/g) plus SD). (b) Mouse whole-body maximum intensity projection. (c) 1T GRE 3D coronal and sagittal MRI, PET, and PET−MR co-registered images of a nude mouse bearing a subcutaneous U87MG-Luc2 human glioblastoma (white arrows) acquired by performing a 45 min dynamic scan following [^{18}F]**20** administration (PET images represent a summation of the last 15 min of the scan). (d) Representative immunohistochemistry images of U87MG-Luc2 subcutaneous tumor and muscle tissue isolated from nude mice stained for PARP-1 and counter-stained with hematoxylin (brown staining signifies the presence of PARP-1, and dark blue staining shows cellular nuclei). (e) Ratio of percentage of injected dose per gram (%ID/g) of tissue of interest to muscle of [^{18}F]**20**, 60 min after injection in subcutaneous U87MG-Luc2 human glioblastoma bearing nude mice pretreated with either vehicle (n = 3) or 50 mg/kg of **1** (n = 3) (error bars represent the mean plus SD; unpaired t-test: $P < 0.05$).

spectra were recorded on a Bruker DPX NMR spectrometer at either 101 or 126 MHz, and data are reported as follows: chemical shift (ppm) relative to Me_4Si or the solvent as internal standard ($CDCl_3$, δ 77.2 ppm; CD_3OD, δ 49.0 ppm; or DMSO-d_6, δ 39.5 ppm), multiplicity with respect to proton (deduced from DEPT experiments; C, CH, CH_2, or CH_3). Infrared spectra were recorded using a Shimadzu IRPrestige-21 spectrometer; wavenumbers are indicated with units of cm^{-1}. Mass spectra were recorded using electron impact, chemical ionization, or electrospray techniques. High-resolution mass spectrometry (HRMS) results were recorded using a JEOL JMS-700 spectrometer. Melting points are uncorrected. All compounds used for biological testing exhibited >95% purity as per HPLC. Purity assessment of compounds **8**−**13** was performed by injecting 0.5−1.5 mg/mL of sample of interest in 1:1 MeCN and 0.01 mM PBS (pH 7.4) onto a reverse-phase Phenomenex Luna 5 μm C18 100 Å (50 mm × 30 mm) column under the following mobile-phase conditions: 0.0−10.5 min, 100:0 to 10:90 A/B; 10.5−11.5 min, 10:90 A/B; and 11.5−12.0 min, 10:90 to 100:0 A/B, where A is PBS (pH 7.4) and B is MeCN. The mobile-phase flow rate was 1.0 mL/min, and the column temperature was set to 25 °C. Analytical UV detection was performed using a UltiMate diode array detector (190−800 nm). Purity assessment for compound **20** was performed as described above using the following mobile-phase conditions: 0.0−15.0 min 70:30 to 5:95 A/B, where A is PBS (pH 7.4) and B is MeCN. Mice used for in vivo studies were housed in individually ventilated cages and had access to sterilized food and water ad libitum. All animal experiments were carried out in compliance with UK Home Office regulations. The synthesis of compounds **1**, **7**, and **15** has been reported previously.[19]

4-[3′-[4″-(4‴-Fluorobenzoyl)piperazine-1″-carbonyl]-4′-fluorobenzyl]-2*H*-phthalazin-1-one (8). To a solution of 4-fluorobenzoic acid (0.029 g, 0.21 mmol) in dichloromethane (5 mL) was added *N*,*N*-diisopropylethylamine (DIPEA; 60.8 μL, 0.349 mmol) followed by 2-(1H-benzotriazol-1-yl)-1,1,3,3-tetramethyluronium hexafluorophosphate (HBTU; 0.080 g, 0.21 mmol), and the mixture was stirred vigorously under reflux for 1 h. Following this, **7** (0.064 g, 0.17 mmol) was added, and the mixture was stirred for a further 24 h. On cooling to ambient temperature, water (5 mL) was added and the organic layer washed with water (3 × 10 mL) and a saturated $NaHCO_3$ solution (10 mL), dried with $MgSO_4$, filtered, and concentrated in vacuo. Purification using flash column chromatography ($MeOH/CH_2Cl_2$, 3:97) gave **8** (0.064 g, 75%) as a white solid; mp 166−168 °C; IR (neat): 3202, 2922, 1629, 1425, 1285, 1223, 1152, 1005, 847 cm^{-1}; ^{1}H NMR (400 MHz, $CDCl_3$, δ): 3.20−4.05 (m, 8H), 4.29 (s, 2H), 6.98−7.14 (m, 3H), 7.30−7.45 (m, 4H), 7.68−7.79 (m, 3H), 8.45−8.49 (m, 1H), 11.37 (s, 1H); ^{13}C NMR (101 MHz, $CDCl_3$, δ): 37.7 (CH_2), 42.1 (2 × CH_2), 47.0 (2 × CH_2), 115.8 (2 × CH, d, J_{C-C-F} = 21.9 Hz), 116.2 (CH, d, J_{C-C-F} = 22.0 Hz), 123.6 (C, d, J_{C-C-F} = 17.8 Hz), 125.0 (CH), 127.2 (CH), 128.3 (C), 129.3 (CH, d, $J_{C-C-C-F}$ = 3.5 Hz), 129.5 (2 × CH, d, $J_{C-C-C-F}$ = 8.7 Hz), 131.1 (C, d, $J_{C-C-C-C-F}$ = 3.5 Hz), 131.6 (CH), 131.8 (CH, d, $J_{C-C-C-F}$ = 8.0 Hz), 133.7 (CH), 134.5 (C, d, $J_{C-C-C-C-F}$ = 3.5 Hz), 145.5 (C), 157.0 (C, d, J_{C-F} = 247.4 Hz), 160.8 (2 × C), 163.6 (C, d, J_{C-F} = 250.7 Hz), 165.2 (C), 169.7 (C); HRMS (ESI): [MNa^+] calcd for $C_{27}H_{22}F_2N_4NaO_3$, 511.1552; found, 511.1547.

4-[3′-[4″-(2‴-Fluorobenzoyl)piperazine-1″-carbonyl]-4′-fluorobenzyl]-2*H*-phthalazin-1-one (9). The reaction was carried out as described for **8** using 2-fluorobenzoic acid (0.047 g, 0.34 mmol), DIPEA (97.0 μL, 0.557 mmol), HBTU (0.127 g, 0.334 mmol), and **7** (0.102 g, 0.278 mmol) in dichloromethane (10 mL). Purification using flash column chromatography ($MeOH/CH_2Cl_2$, 3:97) gave **9** (0.072 g, 53%) as a white solid. NMR spectra showed a 56:44 mixture of rotamers. Only the data for the major rotamer were recorded; mp 246−248 °C; IR (neat): 3043, 2894, 1684, 1641, 1464, 1433, 1289, 1251, 1007, 775 749 cm^{-1}; ^{1}H NMR ($CDCl_3$, 400 MHz) δ 3.20−4.10 (m, 8H), 4.30 (s, 2H), 6.96−7.50 (m, 7H), 7.67−7.81 (m, 3H), 8.42−8.49 (m, 1H), 10.17 (br s, 1H); ^{13}C NMR ($CDCl_3$, 101 MHz) δ 37.7 (CH_2), 41.8 (CH_2), 42.2 (CH_2), 46.8 (CH_2), 47.4 (CH_2), 115.9 (CH, d, J_{C-C-F} = 21.4 Hz), 116.1 (CH, d, J_{C-C-F} = 20.4 Hz), 123.4 (C, d, J_{C-C-F} = 17.8 Hz), 123.7 (C, d, J_{C-C-F} = 18.3 Hz), 125.0 (CH), 125.0 (2 × CH), 127.3 (CH), 128.4 (C), 129.3 (CH), 129.5 (C), 131.7 (CH), 131.8 (CH), 131.9 (CH), 133.7 (2 × CH), 134.4 (C), 145.5 (C), 157.1 (C, d, J_{C-F} = 247.5 Hz), 158.1 (C, d, J_{C-F} = 247.8 Hz),

DOI: 10.1021/acs.jmedchem.8b00138
J. Med. Chem. 2018, 61, 4103−4114

160.1 (C), 165.2 (C), 165.5 (C); HRMS (ESI): [MNa^+] calcd for $C_{27}H_{22}F_2N_4NaO_3$, 511.1552; found, 511.1545.

4-[3′-[4″-(4‴-Fluoro-2‴-methylbenzoyl)piperazine-1″-carbonyl]-4′-fluorobenzyl]-2*H*-phthalazin-1-one (10). To a solution of 4-fluoro-2-methylbenzoic acid (0.042 g, 0.27 mmol) in dichloromethane (5 mL) was added EDCI (0.052 g, 0.27 mmol), and the reaction mixture was stirred at ambient temperature for 0.5 h. 4-Dimethylaminopyridine (DMAP; 0.017 g, 0.14 mmol) was then added and the mixture was stirred for a further 0.5 h. A solution of **7** (0.100 g, 0.273 mmol) in dichloromethane (5 mL) was then added drop-wise and the resultant reaction mixture stirred vigorously under reflux for 24 h. Upon cooling to ambient temperature, water (5 mL) was added and the organic layer washed with water (3 × 5 mL) and a $NaHCO_3$ solution (5 mL), dried with $MgSO_4$, filtered, and concentrated in vacuo. Purification using flash column chromatography (MeOH/CH_2Cl_2, 1:49) gave **10** (0.043 g, 31%) as a white solid. NMR spectra showed a 59:41 mixture of rotamer. Only data for the major rotamers were recorded; mp 175−177 °C; IR (neat): 3188, 2926, 1632, 1462, 1429, 1256, 1159, 1003, 772, 727 cm^{-1}; ^1H NMR (400 MHz, $CDCl_3$, δ): 2.32 (s, 3H), 3.15−3.45 (m, 4H), 3.55−4.10 (m, 4H), 4.30 (s, 2H), 6.85−7.18 (m, 4H), 7.26−7.39 (m, 2H), 7.67−7.81 (m, 3H), 8.43−8.50 (m, 1H), 10.30 (s, 1H); ^{13}C NMR (126 MHz, $CDCl_3$, δ): 19.2 (CH_3), 37.7 (CH_2), 41.8 (CH_2), 42.4 (CH_2), 46.5 (CH_2), 46.9 (CH_2), 113.2 (CH, d, J_{C-C-F} = 21.5 Hz), 116.3 (CH, d, J_{C-C-F} = 20.6 Hz), 117.5 (CH, d, J_{C-C-F} = 21.1 Hz), 123.6 (C, d, J_{C-C-F} = 17.0 Hz), 125.0 (CH), 127.2 (CH), 127.8 (CH, d, $J_{C-C-C-F}$ = 8.6 Hz), 128.3 (C), 129.3 (CH, d, $J_{C-C-C-F}$ = 3.2 Hz), 129.6 (C), 131.5 (C, d, $J_{C-C-C-C-F}$ = 7.3 Hz), 131.6 (CH), 131.8 (CH), 133.7 (CH), 134.5 (C, d, $J_{C-C-C-C-F}$ = 3.4 Hz), 137.4 (C, d, $J_{C-C-C-F}$ = 8.1 Hz), 145.5 (C), 157.0 (C, d, J_{C-F} = 246.4 Hz), 160.7 (C), 162.9 (C, d, J_{C-F} = 248.8 Hz), 165.3 (C), 169.6 (C); HRMS (ESI): [MNa^+] calcd for $C_{28}H_{24}F_2N_4NaO_3$, 525.1709; found, 525.1696.

4-[3′-[4″-[(4‴-Fluorophenyl)acetyl]piperazine-1″-carbonyl]-4′-fluorobenzyl]-2*H*-phthalazin-1-one (11). To a solution of 4-fluorophenylacetic acid (0.043 g, 0.28 mmol) in dimethylformamide (DMF; 5 mL) was added DIPEA (93.4 μL, 0.546 mmol) followed by HBTU (0.105 g, 0.277 mmol), and the reaction mixture was stirred vigorously at ambient temperature for 1 h. A solution of **7** (0.100 g, 0.273 mmol) in DMF (5 mL) was then added drop-wise, and the resultant reaction mixture heated to and stirred at 50 °C for a further 24 h. The crude reaction mixture was worked up as described for as described for **8**. Purification using flash column chromatography (MeOH/CH_2Cl_2, 1:24) gave **11** (0.063 g, 46%) as white solid. NMR spectra showed a 57:43 mixture of rotamers. Only data for the major rotamer were recorded; mp 216−218 °C; IR (neat): 2899, 2346, 1636, 1586, 1508, 1431, 1219, 1157, 1011 cm^{-1}; ^1H NMR (400 MHz, $CDCl_3$, δ): 3.03−3.85 (m, 10H), 4.28 (br s, 2H), 6.95−7.07 (m, 3H), 7.13−7.24 (m, 2H), 7.27−7.36 (m, 2H), 7.66−7.79 (m, 3H), 8.44−8.49 (m, 1H), 11.01 (s, 1H); ^{13}C NMR (101 MHz, $CDCl_3$, δ): 37.7 (CH_2), 39.9 (CH_2), 42.0 (2 × CH_2), 45.7 (CH_2), 46.7 (CH_2), 115.7 (2 × CH, d, J_{C-C-F} = 21.4 Hz), 116.2 (CH, d, J_{C-C-F} = 22.0 Hz), 123.5 (C, d, J_{C-C-F} = 17.6 Hz), 125.0 (CH), 127.2 (CH), 128.3 (C), 129.2 (CH, d, $J_{C-C-C-F}$ = 2.3 Hz), 129.5 (C), 130.2 (C), 130.2 (2 × CH, d, $J_{C-C-C-F}$ = 7.9 Hz), 131.6 (CH), 131.8 (CH, d, $J_{C-C-C-F}$ = 8.1 Hz), 133.7 (CH), 134.5 (C, d, $J_{C-C-C-C-F}$ = 3.4 Hz), 145.5 (C), 157.0 (C, d, J_{C-F} = 247.6 Hz), 160.8 (C), 161.9 (C, d, J_{C-F} = 247.6 Hz), 165.2 (C), 169.6 (C); HRMS (ESI): [MNa^+] calcd for $C_{28}H_{24}F_2N_4NaO_3$, 525.1709; found, 525.1705.

4-[3′-[4‴′-[(4‴-Fluorophenyl)butane-1‴′,4‴′-dione]-piperazine-1‴-carbonyl]4″-fluorobenzyl]-2*H*-phthalazin-1-one (12). The reaction was carried out as described for **10** using 3-(4-fluorobenzoyl)propionic acid (0.053 g, 0.27 mmol), 1-ethyl-3-(3-dimethylaminopropyl)carbodiimide (EDCI; 0.052 g, 0.27 mmol), DMAP, and **7** (0.100 g, 0.273 mmol) in dichloromethane (10 mL). Purification using flash column chromatography (MeOH/CH_2Cl_2, 1:24) gave **12** (0.050 g, 34%) as a pale yellow solid. NMR spectra showed a 56:44 mixture of rotamers. Only data for the major rotamer were recorded; mp 128−130 °C; IR (neat): 3208, 2909, 1636, 1595, 1433, 1356, 1225, 1155, 1011 cm^{-1}; ^1H NMR (400 MHz, $CDCl_3$, δ): 2.82 (t, J = 6.4 Hz, 2H), 3.24−3.46 (m, 4H), 3.50−3.98 (m, 6H), 4.28 (s, 2H), 7.05 (t, J = 8.8 Hz, 1H), 7.10−7.16 (m, 2H), 7.30−7.39 (m, 2H), 7.68−7.81 (m, 3H), 8.00−8.06 (m, 2H), 8.44−8.49 (m, 1H), 10.33 (s, 1H); ^{13}C NMR (101 MHz, $CDCl_3$, δ): 27.0 (CH_2), 33.4 (CH_2), 37.7 (CH_2), 42.0 (CH_2), 42.1 (CH_2), 45.1 (CH_2), 46.8 (CH_2), 115.7 (2 × CH, d, J_{C-C-F} = 21.8 Hz), 116.2 (CH, d, J_{C-C-F} = 21.9 Hz), 123.7 (C, d, J_{C-C-F} = 17.6 Hz), 125.0 (CH), 127.2 (CH), 128.3 (C), 129.2 (CH, d, $J_{C-C-C-F}$ = 3.0 Hz), 129.6 (C), 130.8 (2 × CH, d, $J_{C-C-C-F}$ = 9.4 Hz), 131.6 (CH), 131.7 (CH, d, $J_{C-C-C-F}$ = 8.0 Hz), 133.2 (C), 133.6 (CH), 134.5 (C, d, $J_{C-C-C-C-F}$ = 3.3 Hz), 145.5 (C), 157.0 (C, d, J_{C-F} = 247.4 Hz), 160.7 (C), 165.3 (C), 165.8 (C, d, J_{C-F} = 254.8 Hz), 170.5 (C), 197.4 (C); HRMS (ESI): [MNa^+] calcd for $C_{30}H_{26}F_2N_4NaO_4$, 567.1814; found, 567.1796.

4-[3′-[4″-(4‴-Fluorobenzyl)piperazine-1″-carbonyl]-4′-fluorobenzyl]-2*H*-phthalazin-1-one (13). To a stirred solution of **7** (0.023 g, 0.063 mmol) in dichloromethane (3 mL) was added 4-fluorobenzyl chloride (7.9 μL, 0.066 mmol) followed by DIPEA (21.9 μL, 0.126 mmol). The resultant reaction mixture was stirred at ambient temperature for 12 h, and then water (5 mL) was added. The mixture was washed with water (2 × 5 mL) and the organic layer was dried with $MgSO_4$, filtered, and concentrated in vacuo. Purification using flash column chromatography (MeOH/CH_2Cl_2, 1:9) gave **13** (0.011 g, 38%) as an off-white solid; mp 109−111 °C; IR (neat): 3185, 2916, 1637, 1508, 1437, 1348, 1221, 1148, 999 cm^{-1}; ^1H NMR (400 MHz, $CDCl_3$, δ): 2.34 (br s, 2H), 2.50 (t, J = 5.2 Hz, 2H), 3.28 (br s, 2H), 3.48 (s, 2H), 3.75−3.82 (m, 2H), 4.28 (s, 2H), 6.96−7.04 (m, 3H), 7.24−7.34 (m, 4H), 7.69−7.78 (m, 3H), 8.44−8.50 (m, 1H), 10.86 (s, 1H); ^{13}C NMR (101 MHz, $CDCl_3$, δ): 37.8 (CH_2), 42.0 (CH_2), 47.1 (CH_2), 52.5 (CH_2), 53.0 (CH_2), 62.0 (CH_2), 115.2 (2 × CH, d, J_{C-C-F} = 21.2 Hz), 116.1 (CH, d, J_{C-C-F} = 21.8 Hz), 124.3 (C, d, J_{C-C-F} = 18.3 Hz), 125.1 (CH), 127.2 (CH), 128.3 (C), 129.1 (CH, d, $J_{C-C-C-F}$ = 3.8 Hz), 129.6 (C), 130.5 (2 × CH, d, $J_{C-C-C-F}$ = 7.9 Hz), 131.2 (CH, d, $J_{C-C-C-F}$ = 7.9 Hz), 131.6 (CH), 133.3 (C, d, $J_{C-C-C-C-F}$ = 3.0 Hz), 133.7 (CH), 134.1 (C, d, $J_{C-C-C-C-F}$ = 3.4 Hz), 145.6 (C), 157.0 (C, d, J_{C-F} = 247.7 Hz), 160.5 (C), 162.1 (C, d, J_{C-F} = 245.0 Hz), 164.8 (C); HRMS (ESI): [MH^+] calcd for $C_{27}H_{25}F_2N_4O_2$, 475.1940; found, 475.1929.

4-[3′-[4″-(4‴-Nitrobenzoyl)piperazine-1″-carbonyl]-4′-fluorobenzyl]-2*H*-phthalazin-1-one (14). To a solution of 4-nitrobenzoic acid (92.0 mg, 0.550 mmol) in DMF (10 mL), was added Et_3N (119 μL, 0.880 mmol), followed by HBTU (231 mg, 0.610 mmol) and the mixture was stirred at room temperature for 1 h. Compound **7** (200 mg, 0.550 mmol) was added, and the mixture was stirred at room temperature for a further 48 h. Water (12 mL) was then added, followed by 1 h of stirring, after which the mixture was cooled to 0 °C. The resulting precipitate was collected by vacuum filtration, washed with water (4 × 20 mL), and dried in vacuo to yield **14** (239 mg, 84%) as an orange foam. NMR spectra showed a 3:2 mixture of rotamers. Only data for the major rotamer were recorded; IR (neat): 3167, 3012, 2904, 1638, 1616, 1599, 1346, 1433, 1265, 1004, 735 cm^{-1}; ^1H NMR (400 MHz, d_6-DMSO, δ): 3.23 (s, 2H), 3.38 (s, 2H), 3.57−3.86 (m, 4H), 4.39 (s, 2H), 7.21−7.34 (m, 1H), 7.35−7.53 (m, 2H), 7.69−7.79 (m, 2H), 7.79−8.05 (m, 3H), 8.25−8.38 (m, 3H), 12.65 (s, 1H); ^{13}C NMR (101 MHz, d_6-DMSO, δ): 37.0 (CH_2), 41.9 (2 × CH_2), 46.9 (2 × CH_2), 116.3 (CH, d, J_{C-C-F} = 18.2 Hz), 123.8 (C, d, J_{C-C-F} = 18.0 Hz), 124.0 (2 × CH), 125.9 (CH), 126.5 (CH), 128.3 (C), 128.8 (2 × CH), 129.4 (CH), 129.5 (C), 132.0 (CH), 132.2 (CH, d, $J_{C-C-C-F}$ = 8.8 Hz), 133.9 (CH), 135.3 (C, d, $J_{C-C-C-C-F}$ = 3.4 Hz), 142.3 (C), 145.2 (C), 148.4 (C), 156.8 (C d, J_{C-F} = 245.7 Hz), 159.8 (C), 164.5 (C), 167.8 (C); HRMS (ESI): [MNa^+] calcd for $C_{27}H_{22}FN_5NaO_5$, 538.1497; found, 538.1488.

***tert*-Butyl Piperazine-4-[[(4′-chloromethyl)benzoyl]-1′carbonyl]-1-carboxylate (16).** The reaction was carried out as described for **14** using a solution of 4-(chloromethyl)benzoic acid (183 mg, 1.07 mmol) in DMF (5 mL), Et_3N (23.1 μL, 1.71 mmol), and HBTU (446 mg, 1.18 mmol). Compound **15** (200 mg, 1.07 mmol) was added, and the mixture was stirred for a further 112 h. After this, water (10 mL) was added and the crude product was extracted into dichloromethane (3 × 10 mL). The organic layers were combined and washed with water (6 × 20 mL), dried with $MgSO_4$, filtered, and concentrated in vacuo to give a white solid. Purification by

DOI: 10.1021/acs.jmedchem.8b00138
J. Med. Chem. 2018, 61, 4103−4114

flash column chromatography (hexane/EtOAc, 1:1) gave **16** as a white solid (144 mg, 40%); mp 140−142 °C; IR (neat): 3003, 2881, 1681, 1622, 1568, 1426, 1349, 1263, 1012, 724, 668 cm^{-1}; ^1H NMR (400 MHz, $CDCl_3$, δ): 1.47 (s, 9H), 3.28−3.84 (m, 8H), 4.60 (s, 2H), 7.43 (q, J = 11.9 Hz, 4H); ^{13}C NMR (101 MHz, $CDCl_3$, δ): 28.5 (3 × CH_3), 43.8 (2 × CH_2), 45.6 (CH_2), 47.7 (2 × CH_2), 80.5 (C), 127.6 (2 × CH), 128.8 (2 × CH), 135.6 (C), 139.4 (C), 154.6 (C), 170.1 (C); HRMS (ESI): [MNa^+] calcd for $C_{17}H_{23}{}^{35}Cl_2N_2NaO_3$, 361.1289; found, 361.1273.

***tert*-Butyl Piperazine-4-[[(4′-fluoromethyl)benzoyl]-1′carbonyl]-1-carboxylate (17).** To a solution of **16** (55.0 mg, 0.162 mmol) in MeCN (1.5 mL) was added a 1 M solution of TBAF (325 μL, 0.325 mmol) in tetrahydrofuran. The mixture was heated to 80 °C and stirred for 1 h followed by evaporation of solvent in vacuo. The crude product was extracted into dichloromethane (5 mL), and the organic layer was washed with water (3 × 10 mL), dried with $MgSO_4$, filtered, and concentrated in vacuo to give **17** (52.0 mg, 100%) as a white solid; mp 96−98 °C; IR (neat): 3013, 2928, 1690, 1630, 1420, 1250, 1009, 909, 756, 731 cm^{-1}; ^1H NMR (400 MHz, $CDCl_3$, δ): 1.45 (s, 9H), 3.25−3.84 (m, 8H), 5.40 (d, J = 47.4 Hz, 2H), 7.37−7.43 (m, 4H); ^{13}C NMR (101 MHz, $CDCl_3$, δ): 28.5 (3 × CH_3), 42.2 (CH_2), 43.7 (2 × CH_2), 47.6 (CH_2), 80.5 (C), 83.9 (CH_2, d, J_{C-F} = 167.6 Hz), 127.4 (2 × CH, d, $J_{C-C-C-F}$ = 6.2 Hz), 127.5 (2 × CH), 135.9 (C, d, $J_{C-C-C-C-C-F}$ = 2.6 Hz), 138.1 (C, d, J_{C-C-F} = 17.4 Hz), 154.6 (C), 170.2 (C); HRMS (ESI): [MNa^+] calcd for $C_{17}H_{23}FN_2NaO_3$, 345.1585; found, 345.1569.

Piperazine-4-[(4′-fluoromethyl)benzoyl]-1′carbonyl (18). To a solution of **17** (52.0 mg, 0.161 mmol) in dichloromethane (1 mL) was added trifluoroacetic acid (124 μL, 1.61 mmol), and the mixture was stirred at room temperature for 4 h. The crude product was extracted into EtOAc (5 mL), and the organic layer was washed using an aqueous saturated solution of potassium carbonate (3 × 10 mL), dried with $MgSO_4$, filtered, and concentrated in vacuo to give **18** (31.0 mg, 87%) as an orange oil; IR (neat): 3411, 3001, 2957, 1613, 1437, 1276, 1263, 1016, 748 cm^{-1}; ^1H NMR (400 MHz, $CDCl_3$, δ): 2.80 (br s, 2H), 2.94 (br s, 2H), 3.38 (br s, 2H), 3.75 (br s, 2H), 5.40 (d, J = 47.5 Hz, 2H), 7.38−7.45 (m, 4H); ^{13}C NMR (101 MHz, $CDCl_3$, δ): 43.3 (CH_2), 46.0 (CH_2), 46.5 (CH_2), 49.0 (CH_2), 84.0 (CH_2, d, J_{C-F} = 167.4 Hz), 127.3 (2 × CH, d, $J_{C-C-C-F}$ = 6.4 Hz), 127.4 (2 × CH), 136.3 (C, d, $J_{C-C-C-C-C-F}$ = 2.8 Hz), 137.7 (C, d, J_{C-C-F} = 17.4 Hz), 170.0 (C); HRMS (ESI): [MNa^+] calcd for $C_{12}H_{15}FN_2NaO$, 245.1061; found, 245.1064.

4-[3′-[4″-(4‴-Fluoromethyl)benzoyl)piperazine-1″-carbonyl]-4′-fluorobenzyl]-2*H*-phthalazin-1-one (20). To a solution of **19** (38.0 mg, 0.126 mmol) in DMF (1 mL) was added Et_3N (26.0 μL, 0.189 mmol), followed by HBTU (52.6 mg, 0.139 mmol), and the mixture was stirred at room temperature for 1 h. Compound **18** (28.0 mg, 0.126 mmol) was added, and the mixture was stirred for a further 72 h. Water (4 mL) was then added, followed by 1 h of stirring, after which the mixture was cooled to 0 °C. The resulting precipitate was collected by vacuum filtration, and the crude orange solid was purified by flash column chromatography (MeOH/EtOAc, 1:19) gave **20** (10.7 mg, 17%) as a yellow foam; IR (neat): 3213, 3005, 2926, 1613, 1572, 1429, 1256, 1225, 1003, 750 cm^{-1}; ^1H NMR (400 MHz, $CDCl_3$, δ): 3.13−4.02 (m, 8H), 4.29 (s, 2H), 5.41 (d, J = 47.3 Hz, 2H), 7.04 (br s, 1H), 7.34 (d, J = 6.2 Hz, 2H), 7.43 (br s, 4H), 7.67−7.72 (m, 1H), 7.73−7.80 (m, 2H), 8.44−8.49 (m, 1H), 10.70 (br s, 1H); ^{13}C NMR (101 MHz, $CDCl_3$, δ): 37.8 (CH_2), 42.3 (2 × CH_2), 47.2 (2 × CH_2), 84.0 (CH_2, d, J_{C-F} = 167.8 Hz), 116.3 (CH, d, J_{C-C-F} = 19.9 Hz), 123.8 (C, d, J_{C-C-F} = 18.2 Hz), 125.1 (CH), 127.4 (CH), 127.5 (2 × CH, d, $J_{C-C-C-F}$ = 6.0 Hz), 127.6 (2 × CH), 128.5 (C), 129.4 (CH, d, $J_{C-C-C-F}$ = 3.7 Hz), 129.7 (C), 131.8 (CH), 132.0 (CH, d, $J_{C-C-C-F}$ = 8.2 Hz), 133.8 (CH), 134.6 (C, d, $J_{C-C-C-C-F}$ = 3.5 Hz), 135.5 (C, d, $J_{C-C-C-C-C-F}$ = 2.8 Hz), 138.5 (C, d, J_{C-C-F} = 17.5 Hz), 145.6 (C), 157.1 (C, d, J_{C-F} = 247.1 Hz), 160.5 (C), 165.3 (C), 170.3 (C); HRMS (ESI): [MNa^+] calcd for $C_{28}H_{24}F_2N_4NaO_3$, 525.1714; found, 525.1738.

4-[3′-[4″-(4‴-Chloromethyl)benzoyl)piperazine-1″-carbonyl]-4′-fluorobenzyl]-2*H*-phthalazin-1-one (21). The reaction was carried out as described for **14** using a solution of 4-(chloromethyl)-benzoic acid (18.7 mg, 0.110 mmol) in DMF (1 mL), Et_3N (24.0 μL, 0.180 mmol) and HBTU (45.6 mg, 0.120 mmol). Following the addition of **7** (40.0 mg, 0.110 mmol) the mixture was stirred at room temperature for a further 72 h. Water (6 mL) was then added, followed by 0.5 h of stirring, after which the mixture was cooled to 0 °C. The resulting precipitate was collected by vacuum filtration and washed with water (4 × 20 mL). Purification by flash column chromatography (MeOH/EtOAc, 1:19) gave **21** (19.0 mg, 34%) as a white foam; IR (neat): 3200, 2924, 1630, 1429, 1256, 1005, 750, 731 cm^{-1}; ^1H NMR (400 MHz, $CDCl_3$, δ): 3.21−3.99 (m, 8H), 4.27 (s, 2H), 4.59 (s, 2H), 7.03 (br s, 1H), 7.30−7.36 (m, 2H), 7.37−7.49 (m, 4H), 7.67−7.72 (m, 1H), 7.73−7.80 (m, 2H), 8.44−8.49 (m, 1H), 10.84 (br s, 1H); ^{13}C NMR (101 MHz, $CDCl_3$, δ): 37.8 (CH_2), 42.3 (2 × CH_2), 45.6 (CH_2), 47.1 (2 × CH_2), 116.3 (CH, d, J_{C-C-F} = 19.9 Hz), 123.8 (C, d, J_{C-C-F} = 17.7 Hz), 125.1 (CH), 127.4 (CH), 127.7 (2 × CH), 128.5 (C), 129.0 (2 × CH), 129.4 (CH, d, $J_{C-C-C-F}$ = 3.6 Hz), 129.7 (C), 131.8 (CH), 132.0 (CH, d, $J_{C-C-C-F}$ = 8.2 Hz), 132.1 (2 × CH), 133.8 (CH), 134.6 (C, d, $J_{C-C-C-C-F}$ = 3.5 Hz), 135.2 (C), 139.7 (C), 145.6 (C), 157.2 (C, d, J_{C-F} = 248.1 Hz), 160.5 (C), 165.3 (C), 170.2 (C); HRMS (ESI): [MNa^+] calcd for $C_{28}H_{24}{}^{35}ClFN_4NaO_3$, 541.1413; found, 541.1413.

4-[3′-[4″-(4‴-Chloromethyl)benzoyl)piperazine-1″-carbonyl]-4′-fluorobenzyl]-2-*tert*-butyloxycarbonylphthalazin-1-one (22). To a solution of **21** (170 mg, 0.328 mmol) in MeCN (1.5 mL) was added di-*tert*-butyl dicarbonate (86.0 mg, 0.393 mmol) and DMAP (4.00 mg, 0.0328 mmol). The mixture was stirred at room temperature for 4 h followed by the evaporation of solvent in vacuo. The crude product was extracted into EtOAc (5 mL), and the organic layer was washed with water (3 × 10 mL), dried with $MgSO_4$, filtered and concentrated in vacuo to give 22 as a white foam (148 mg, 72%); IR (neat): 2982, 1634, 1427, 1248, 1003, 750 cm^{-1}; ^1H NMR (400 MHz, $CDCl_3$, δ): 1.66 (s, 9H), 3.15−3.99 (m, 8H), 4.30 (s, 2H), 4.59 (s, 2H), 7.03 (br s, 1H), 7.30−7.36 (m, 2H), 7.37−7.49 (m, 4H), 7.59−7.67 (m, 1H), 7.69−7.78 (m, 2H), 8.42−8.49 (m, 1H); ^{13}C NMR (101 MHz, $CDCl_3$, δ): 27.8 (3 × CH_3), 38.1 (CH_2), 42.2 (2 × CH_2), 45.4 (CH_2), 47.1 (2 × CH_2), 85.9 (C), 116.2 (CH, d, J_{C-C-F} = 20.4 Hz), 123.7 (C, d, J_{C-C-F} = 18.2 Hz), 125.1 (CH), 127.6 (2 × CH), 128.1 (CH), 128.7 (C), 128.8 (2 × CH), 129.1 (C), 129.2 (CH, d, $J_{C-C-C-F}$ = 3.4 Hz), 131.8 (CH, d, $J_{C-C-C-F}$ = 7.6 Hz), 132.0 (CH), 134.0 (CH), 134.1 (C, d, $J_{C-C-C-C-F}$ = 3.7 Hz), 135.1 (C), 139.5 (C), 145.3 (C), 151.1 (C), 157.0 (C, d, J_{C-F} = 247.7 Hz), 158.2 (C), 165.1 (C), 170.0 (C); HRMS (ESI): [MNa^+] calcd for $C_{33}H_{32}{}^{35}ClFN_4NaO_5$, 641.1937; found, 641.1915.

In Vitro Characterization. Lipophilicity (log P_{oct}) and percentage plasma protein binding values and the cell-free IC_{50} parameter for compounds **8**−**13** and **20** were obtained using previously described HPLC and colorimetric dose−response methodologies, respectively.[19] Similarly, the cellular IC_{50} parameter of **8** and **20** and the plasma stability and intrinsic clearance parameters of compound **20** were established using previously reported methods.[19] Correlation of cellular fluorescence IC_{50} data with cell-free colorimetric IC_{50} data was used to eliminate potential fluorescence assay interference mechanisms.

Generation of $^{18}F^-/H_2{}^{18}O$. [^{18}F]fluoride was generated via the [$^{18}O(p, n)^{18}F$] nuclear reaction by irradiating [^{18}O]water using a 16.5 MeV proton beam (40 μA) produced by a PETtrace 6 cyclotron unit.

Manual Radiosynthesis of [^{18}F]8. A stock solution of K_{222}/K_2CO_3 (0.25 mL), prepared by dissolving 100.0 mg of K_{222} (0.266 mmol) in 2 mL of MeCN and adding 12.0 mg of K_2CO_3 (0.087 mmol) in 0.5 mL of distilled water, was added to a 2 mL v-vial containing approximately 100 MBq of $^{18}F^-/H_2{}^{18}O$ (0.25 mL). The [^{18}F]fluoride was dried by passing a constant stream of argon over the solution at 100 °C for approximately 20 min; anhydrous MeCN was added in three aliquots of 0.50 mL to facilitate azeotropic drying. A solution of **14** (1.0−5.0 mg, 0.0019−0.0095 mmol) in anhydrous *N*-methyl-2-pyrrolidone (0.3 mL) was then added to the v-vial, and the reaction was allowed to proceed for 30 min at 180 °C.

Manual Radiosynthesis of [^{18}F]20. A stock solution of 0.750 M $TBAHCO_3$ was prepared by diluting 2.5 mL of 1.5 M TBAOH with 2.5 mL of distilled water; CO_2 was bubbled through the solution for 2

DOI: 10.1021/acs.jmedchem.8b00138
J. Med. Chem. 2018, 61, 4103−4114

h until pH 7.7 was reached, followed by the removal of excess CO_2 by bubbling argon through the mixture until pH 9.0 was reached. The 0.750 M $TBAHCO_3$ solution (10 μL) was added to a 2 mL v-vial containing 469−572 MBq of $^{18}F^-/H_2{}^{18}O$ (0.16 mL). The mixture was vortexed, and the[^{18}F]fluoride was dried by passing a constant stream of argon over the solution at 100 °C for approximately 20 min; anhydrous MeCN was added in three aliquots of 0.50 mL to facilitate azeotropic drying. A solution of **22** (4.9 mg, 0.0079 mmol) in anhydrous MeCN (0.1 mL) and *t*BuOH (0.2 mL) was then added to the v-vial, and the reaction was allowed to proceed for 30 min at 110 °C. After this, distilled water was added (0.45 mL), and the reaction was heated at 120 °C for a further 5 min. Next, the crude reaction mixture was cooled to room temperature, purified using HPLC, and concentrated in vacuo in an evaporator flask. The flask was rinsed with MeCN (3 × 0.3 mL) to extract the radiolabeled compound, and the solution was transferred to a 2 mL v-vial; the solvent was removed by passing a constant stream of argon over the solution at 100 °C for approximately 15 min. The radiotracer was reconstituted in up to 0.65 mL of 5% v/v DMSO in 0.9% w/v saline. The total radiosynthetic time was 138 ± 16 min (n = 6).

HPLC Analysis and Purification of Radiotracers. All radiochemical yields were determined by analytical radio-HPLC of the crude product. Radioactivity yield was determined using the measured radioactivity of the isolated product. Analytical and preparatory Dionex UltiMate 300 series HPLC systems with Phenomenex Synergi 4 μm Hydro-RP 80 Å 150 mm × 4.60 mm and 150 mm × 10 mm columns, respectively, were used. Column temperatures were set to 25 °C, and mobile-phase flow rates were 1 and 3 mL/min for the analytical and preparatory systems, respectively. Analytical UV detection was performed using a UltiMate diode array detector (190−800 nm), and radiodetection was achieved using a Berthold Technologies Flow Star LB513 detector. Preparatory UV detection was performed using a Knauer Advanced Scientific Instruments Smartline UV Detector 2500, and radiodetection was achieved using a pin-diode connected to a Lab Logic Flow-Count radiodetector. Analysis of [^{18}F]**8**, [^{18}F]**20**, and [^{18}F]**23** were performed on crude reaction mixtures that were cooled to room temperature. [^{18}F]**8** was analyzed using the following mobile-phase conditions: 0.0−20.0 min, 30:70 A/B to 55:45 A/B; 20.0−20.5 min, 55/45 A:B to 5:95 A/B; and 20.5−25.0 min, 5:95 A/B, where A is MeCN and B is distilled water. [^{18}F]**20** and [^{18}F]**23** was analyzed using the following mobile-phase conditions: 0.0−15.0 min, 30:70 A/B to 90:10; 15.0−20.0 min, 90:10 A/B; 20.0−20.5 min, 90:10 to 30:70 A/B; and 20.5−25.0 min, 30:70 A/B, where A is MeCN and B is distilled water. Purification of [^{18}F]**20** was performed using the following mobile-phase conditions: 0.0−3.0 min, 30:70 A/B; 3.0−30.0 min, 30:70 to 75:25 A/B; 30.0−30.1 min, 75:25 to 95:5 A/B; and 30.1−35.0 min, 95:5 A/B, where A is MeCN and B is distilled water; the radiolabeled product was collected at approximately 13.5 min. To confirm the identity of the radiolabeled products, the retention times of [^{18}F]**8**, [^{18}F]**20**, and [^{18}F]**23** were compared with the retention times obtained for nonradioactive **8**, **20**, and **23** using the same chromatographic conditions. Because the amount of [^{18}F]**20** that was produced fell below the sensitivity threshold of the UV detector (<1.68 × 10^{-4} μmol), molar activity (Ci/μmol) was calculated using the lowest detectable amount of nonlabeled **20** established from a calibration plot of a range of concentrations (0.001−1.000 mg/mL). All HPLC data acquisition and analyses were carried out using the Chromeleon 6.8 Chromatography software.

Mouse Glioblastoma Model. U87MG-Luc2 glioblastoma cell culture and implantation procedures were performed as reported previously.[19] Briefly, U87MG-Luc2 cells were purchased commercially from ATCC and cultured in minimum essential media that has been supplemented with 10% w/v fetal calf serum and 2 mM L-glutamine at 37 °C and 5% v/v CO_2. Unconscious female CD1 nude mice (6−11 week old; purchased from Charles River Laboratories) had 5 × 10^6 U87MG-Luc2 cells injected subcutaneously into the right flank. The resulting tumor xenografts were measured and monitored visually every 3 days, and tumor-bearing animals were used for in vivo studies 28−30 days post-implantation.

Ex Vivo Biodistribution with and without Preblockade. Subcutaneous tumor bearing mice were administered 1.8−2.6 MBq of [^{18}F]**20** in 0.11−0.21 mL of 5% v/v DMSO in 0.9% saline via bolus tail-vein injections. The remainder of the experiment was conducted as described previously.[19]

PET−MR Imaging. A single subcutaneous U87MG-Luc2 tumor bearing female CD1 nude mouse was anaesthetized using inhaled isoflurane (in medical air; induction 5% v/v; maintenance 2.0−2.5% v/v) and placed in the nanoScan PET−MRI scanner (Mediso Medical Imaging Systems). The mouse received a bolus tail-vein injection of 2.2 MBq of [^{18}F]**20** in 5% v/v DMSO in 0.9% saline, and a 45 min dynamic PET scan (continuous list mode) was initiated immediately after. This was followed by a whole-body 1T GRE 3D Cor/Sag MRI scan. The dynamic PET data were corrected for random coincidences, dead time, scatter, and decay and subsequently reconstructed using 3D Tera-Tomo (Mediso). The reconstructed PET data were automatically co-registered with the MRI data, and they were subsequently analyzed using the PMOD 3.504 software. The PET frames from the last 15 min of the scan were summed to allow for better visual representation of radiotracer biodistribution. Standardized uptake values (SUV) were determined by dividing the image radiotracer concentration by the injected dose divided by the animal weight.

Immunohistochemistry. Tumor and muscle tissue was prepared and stained using anti-PARP-1 antibody (mouse antihuman and mouse antibody; sc-8007; Santa Cruz), as reported previously.[19] Haematoxylin and eosin and Ki67 staining were performed using a Leica ST5020 multi-stainer. Histology images were acquired using a Zeiss AX10 brightfield microscope at a 5× magnification.

■ ASSOCIATED CONTENT

Supporting Information

The Supporting Information is available free of charge on the ACS Publications website at DOI: 10.1021/acs.jmedchem.8b00138.

Molecular formula strings for compounds presented in the manuscript. (CSV)

^{1}H and ^{13}C NMR spectra for all new compounds, cell-free and cellular IC_{50} curves, metabolic stability graphs, radiofluorination optimization, optimization of deprotection chemistry, immunohistochemical staining of the U87MG-Luc2 subcutaneous xenograft, radiochemistry HPLC chromatograms, and purity assessment HPLC chromatograms for key compounds. (PDF)

■ AUTHOR INFORMATION

Corresponding Author

*E-mail: filipzmuda@gmail.com. Phone: +44-(0)1413304924.

ORCID

Filip Zmuda: 0000-0003-3710-0622

Maria Clara Liuzzi: 0000-0002-6121-899X

Andrew Sutherland: 0000-0001-7907-5766

Notes

The authors declare the following competing financial interest(s): Partial funding received from AstraZeneca, who are patent holders for the PARP inhibitor olaparib.

■ ACKNOWLEDGMENTS

The authors acknowledge Dr. Shafiq Ahmed for providing guidance concerning the cellular IC_{50} assays and Dr. Lesley Gilmour and Sandeep Chahal for their input in setting up the necessary small-animal xenograft models. The authors also gratefully acknowledge financial support from the University of Glasgow (studentship FZ), EPSRC (EP/J500434), the Cancer Research U.K. Glasgow Centre Development Fund, The

DOI: 10.1021/acs.jmedchem.8b00138
J. Med. Chem. 2018, 61, 4103−4114

Neuroscience Foundation, The Beatson Cancer Charity, AstraZeneca, and the Scottish Imaging Network: A Platform for Scientific Excellence.

■ ABBREVIATIONS USED

ATCC, American type culture collection; BBB, blood−brain barrier; BRCA, breast cancer; Cl_{int}, intrinsic clearance; IC_{50}, half-maximum inhibitory concentration; ID/g, injected dose per gram of material; K_{222}, Kryptofix; log P_{oct}, lipophilicity; MBq, megabequerel; MR, magnetic resonance; MRI, magnetic resonance imaging; PARP, poly(ADP-ribose) polymerase; PARP-1, poly(ADP-ribose) polymerase-1; PPB, plasma-protein binding; PTA, phase-transfer agent; SD, standard deviation; SUV, standardized uptake value; *t*-BuOH, *tert*-butyl alcohol; TBAF, tetra-*n*-butylammoniumfluorine; $TBAHCO_3$, tetra-*n*-butylammonium hydrogen carbonate

■ REFERENCES

(1) Amé, J.; Spenlehauer, C.; de Murcia, G. The PARP superfamily. *BioEssays* **2004**, *26*, 882−893.
(2) Bürkle, A. Poly(ADP-ribose) the most elaborate metabolite of NAD^+. *FEBS J.* **2005**, *272*, 4576−4589.
(3) U.S. Food and Drug Administration. *Orange Book: Approved Drug Products with Therapeutic Equivalence Evaluations*. https://www.accessdata.fda.gov/scripts/cder/ob/index.cfm (accessed Mar 8, 2018).
(4) European Medicines Agency. *European public assessment reports*. http://www.ema.europa.eu/ema/index.jsp?curl=pages/medicines/landing/epar_search.jsp&mid=WC0b01ac058001d124 (accessed Mar 8, 2018).
(5) Ledermann, J. A.; Harter, P.; Gourley, C.; Friedlander, M.; Vergote, I.; Rustin, G.; Scott, C. L.; Meier, W.; Shapira-Frommer, R.; Safra, T.; Matei, D.; Fielding, A.; Spencer, S.; Dougherty, B.; Orr, M.; Hodgson, D.; Barrett, J. C.; Matulonis, U. Olaparib maintenance therapy in patients with platinum-sensitive relapsed serous ovarian cancer: a preplanned retrospective analysis of outcomes by BRCA status in a randomised phase 2 trial. *Lancet Oncol.* **2014**, *15*, 852−861.
(6) Ledermann, J. A.; Harter, H.; Gourley, C.; Friedlander, M.; Vergote, I.; Rustin, G.; Scott, C.; Meier, W.; Shapira-Frommer, R.; Safra, T.; Matei, D.; Fielding, A.; Spencer, S.; Rowe, P.; Lowe, E.; Hodgson, D.; Sovak, M. A.; Matulonis, U. Overall survival in patients with platinum-sensitive recurrent serous ovarian cancer receiving olaparib maintenance monotherapy: an updated analysis from a randomised, placebo-controlled, double-blind, phase 2 trial. *Lancet Oncol.* **2016**, *17*, 1579−1589.
(7) U.S. Food and Drug Administration. *FDA approves olaparib for germline BRCA-mutated metastatic breast cancer*. https://www.fda.gov/Drugs/InformationOnDrugs/ApprovedDrugs/ucm592357.htm (accessed Mar 24, 2018).
(8) U.S. Food and Drug Administration. *FDA approves olaparib tablets for maintenance treatment in ovarian cancer*. https://www.fda.gov/Drugs/InformationOnDrugs/ApprovedDrugs/ucm572143.htm (accessed March 24, 2018).
(9) Ledermann, J. A.; Harter, P.; Gourley, C.; Friedlander, M.; Vergote, I.; Rustin, G.; Scott, C.; Meier, W.; Shapira-Frommer, R.; Safra, T.; Matei, D.; Macpherson, E.; Watkins, C.; Carmichael, J.; Matulonis, U. Olaparib maintenance therapy in platinum-sensitive relapsed ovarian cancer. *N. Engl. J. Med.* **2012**, *366*, 1382−1392.
(10) Robson, M.; Im, S. A.; Senkus, E.; Xu, B.; Domchek, S. M.; Masuda, N.; Delaloge, S.; Li, W.; Tung, N.; Armstrong, A.; Wu, W.; Goessl, C.; Runswick, S.; Conte, P. Olaparib for metastatic breast cancer in patients with a germline BRCA mutation. *N. Engl. J. Med.* **2017**, *377*, 523−533.
(11) Evans, T.; Matulonis, U. PARP inhibitors in ovarian cancer: evidence, experience and clinical potential. *Ther. Adv. Med. Oncol.* **2017**, *9*, 253−267.
(12) Chalmers, A.; Jackson, A.; Swaisland, H.; Stewart, W.; Halford, S. E. R.; Molife, L. R.; Hargrave, D.; McCormick, A. Results of stage 1 of the operatic trial: a phase I study of olaparib in combination with Temozolomide in patients with relapsed glioblastoma [abstract]. *J. Clin. Oncol.* **2014**, *32*, 2025.
(13) Roelcke, U.; Radü, E. W.; von Ammon, K.; Hausmann, O.; Maguire, R. P.; Leenders, K. L. Alteration of blood-brain barrier in human brain tumors: comparison of [18F]fluorodeoxyglucose, [11C]methionine and rubidium-82 using PET. *J. Neurol. Sci.* **1995**, *132*, 20−27.
(14) Kracht, L. W.; Miletic, H.; Busch, S.; Jacobs, A. H.; Voges, J.; Hoevels, M.; Klein, J. C.; Herholz, K.; Heiss, W. D. Delineation of brain tumour extent with [11C]L-methionine positron emission tomography: local comparison with stereotactic histopathology. *Clin. Cancer Res.* **2004**, *10*, 7163−7170.
(15) Wolburg, H.; Noell, S.; Fallier-Becker, P.; Mack, A.; Wolburg-Buchholz, K. The disrupted blood-brain barrier in human glioblastoma. *Mol. Aspects Med.* **2012**, *33*, 579−589.
(16) Rottenberg, S.; Jaspers, J. E.; Kersbergen, A.; van der Burg, E.; Nygren, A. O.; Zander, S. A.; Derksen, P. W.; de Bruin, M.; Zevenhoven, J.; Boulter, R.; Cranston, A.; O'Connor, M. J.; Martin, N. M.; Borst, P.; Jonkers, J.; Lau, A. High sensitivity of BRCA1-deficient mammary tumors to the PARP inhibitor AZD2281 alone and in combination with platinum drugs. *Proc. Natl. Acad. Sci. U. S. A.* **2008**, *105*, 17079−17084.
(17) Carney, B.; Kossatz, S.; Lok, B. H.; Schneeberger, V.; Gangangari, K. K.; Pillarsetty, N. V. K.; Weber, W. A.; Rudin, C. M.; Poirier, J. T.; Reiner, T. Target engagement imaging of PARP inhibitors in small-cell lung cancer. *Nat. Commun.* **2018**, *9*, 176.
(18) Makvandi, M.; Pantel, A.; Schwartz, L.; Schubert, E.; Xu, K.; Hsieh, C.; Hou, C.; Kim, H.; Weng, C.; Winters, H.; Doot, R.; Farwell, M. D.; Pryma, D. A.; Greenberg, R. A.; Mankoff, D. A.; Simpkins, F.; Mach, R. H.; Lin, L. L. A PET imaging agent for evaluating PARP-1 expression in ovarian cancer. *J. Clin. Invest.* **2018**, 1 DOI: 10.1172/JCI97992.
(19) Zmuda, F.; Malviya, G.; Blair, A.; Boyd, M.; Chalmers, A.; Sutherland, A.; Pimlott, S. L. Synthesis and evaluation of a radioiodinated tracer with specificity for poly(ADP-ribose) polymerase-1 (PARP-1) in vivo. *J. Med. Chem.* **2015**, *58*, 8683−8693.
(20) Khalil, M.; Tremoleda, J.; Bayomy, T.; Gsell, W. Molecular SPECT imaging: an overview. *Int. J. Mol. Imaging* **2011**, *2011*, 796025.
(21) Rahmim, A.; Zaidi, H. PET versus SPECT: strengths, limitations and challenges. *Nucl. Med. Commun.* **2008**, *29*, 193−207.
(22) Carney, B.; Kossatz, S.; Reiner, T. Molecular imaging of PARP. *J. Nucl. Med.* **2017**, *58*, 1025−1030.
(23) Knight, J.; Koustoulidou, S.; Cornelissen, B. Imaging the DNA damage response with PET and SPECT. *Eur. J. Nucl. Med. Mol. Imaging* **2017**, *44*, 1065−1078.
(24) Pantel, A.; MaKvandi, M.; Doot, R.; Schwartz, L.; Greenberg, R.; Simpkins, F.; Mankoff, D.; Lin, L.l; Mach, R. A pilot study of a novel poly(ADP-ribose) polymerase-1 (PARP) PET tracer ([^{18}F]-FluorThanatrace) in patients with ovarian carcinoma. *J. Nucl. Med.* **2017**, *58* (1), 386.
(25) Reiner, T.; Lacy, J.; Keliher, J.; Yang, S.; Ullal, A.; Kohler, H.; Vinegoni, C.; Weissleder, R. Imaging therapeutic PARP inhibition in vivo through bioorthogonally developed companion imaging agents. *Neoplasia* **2012**, *14*, 169−177.
(26) Cockcroft, X. L.; Dillon, J.; Dixon, L.; Drzewiecki, J.; Kerrigan, F.; Loh, V. M.; Martin, N. M.; Menear, K. A.; Smith, G. C. Phthalazinones 2: optimization and synthesis of novel potent inhibitors of poly(ADP-ribose)polymerase. *Bioorg. Med. Chem. Lett.* **2006**, *16*, 1040−1044.
(27) Menear, K. A.; Adcock, C.; Boulter, R.; Cockcroft, X. L.; Copsey, L.; Cranston, A.; Dillon, K. J.; Drzewiecki, J.; Garman, S.; Gomez, S.; Javaid, H.; Kerrigan, F.; Knights, C.; Lau, A.; Loh, V. M.; Matthews, I. T.; Moore, S.; O'Connor, M. J.; Smith, G. C.; Martin, N. M. 4-[3-(4-Cyclopropanecarbonylpiperazine-1-carbonyl)-4-fluorobenzyl]2H-phthalazin-1-one: a novel bioavailable inhibitor of poly(ADP-ribose) polymerase-1. *J. Med. Chem.* **2008**, *51*, 6581−6591.
(28) Helmer, F.; Kiehs, K.; Hansch, C. The linear free-energy relationship between partition coefficients and the binding and

DOI: 10.1021/acs.jmedchem.8b00138
J. Med. Chem. 2018, 61, 4103−4114

conformational perturbation of macromolecules by small organic compounds. *Biochemistry* **1968**, *7*, 2858−2863.
(29) Jacobson, O.; Chen, X. Interrogating tumor metabolism and tumor microenvironments using molecular positron emission tomography imaging. Theranostic approaches to improve therapeutics. *Pharmacol. Rev.* **2013**, *65*, 1214−1256.
(30) Tavares, A.; Lewsey, J.; Dewar, D.; Pimlott, S. Radiotracer properties by high performance liquid chromatography: a potential tool for brain radiotracer discovery. *Nucl. Med. Biol.* **2012**, *39*, 127−135.
(31) Lee, S. J.; Oh, S. J.; Chi, D. Y.; Lee, B. S.; Ryu, J. S.; Moon, D. H. Comparison of synthesis yields of 3′-deoxy-3′-[18F]fluorothymidine by nucleophilic fluorination in various alcohol solvents. *J. Labelled Compd. Radiopharm.* **2008**, *51*, 80−82.
(32) Kim, W.; Jeong, H.; Lim, T.; Sohn, M.; Katzenellenbogen, A.; Chi, Y. Facile nucleophilic fluorination reactions using tert-alcohols as a reaction medium: significantly enhanced reactivity of alkali metal fluorides and improved selectivity. *J. Org. Chem.* **2008**, *73*, 957−962.
(33) Salinas, B.; Irwin, P.; Kossatz, S.; Bolaender, A.; Chiosis, G.; Pillarsetty, N.; Weber, W. A.; Reiner, T. Radioiodinated PARP1 tracers for glioblastoma imaging. *EJNMMI Res.* **2015**, *5*, 1−14.
(34) Carney, B.; Carlucci, G.; Salinas, B.; Di Gialleonardo, D.; Kossatz, S.; Vansteene, A.; Longo, V. A.; Bolaender, A.; Chiosis, G.; Keshari, K. R.; Weber, W. A.; Reiner, T. Non-invasive PET imaging of PARP1 expression in glioblastoma models. *Mol. Imaging Biol.* **2016**, *18*, 386−392.
(35) Pike, V. W. PET radiotracers: crossing the blood-brain barrier and surviving metabolism. *Trends Pharmacol. Sci.* **2009**, *30*, 431−440.

DOI: 10.1021/acs.jmedchem.8b00138
J. Med. Chem. 2018, 61, 4103−4114